Monthly Notices
of the
ROYAL ASTRONOMICAL SOCIETY

Mon. Not. R. Astron. Soc. **403,** 2077–2087 (2010) doi:10.1111/j.1365-2966.2010.16248.x

On the overconcentration problem of strong lensing clusters

M. Sereno,[1,2]★ Ph. Jetzer[1] and M. Lubini[1]

[1]*Institut für Theoretische Physik, Universität Zürich, Winterthurerstrasse 190, 8057 Zürich, Switzerland*
[2]*Dipartimento di Fisica, Politecnico di Torino, Corso Duca degli Abruzzi 24, 10129 Torino, Italy*

Accepted 2009 December 22. Received 2009 December 14; in original form 2009 September 25

ABSTRACT

Λ cold dark matter paradigm predicts that galaxy clusters follow a universal mass density profile and fit a well-defined mass–concentration relation, with lensing clusters being preferentially triaxial haloes elongated along the line of sight. Oddly, recent strong and weak lensing analyses of clusters with a large Einstein radius suggested those haloes to be highly overconcentrated. Here, we investigate what intrinsic shape and orientation a halo should have to account for both theoretical predictions and observations. We considered a sample of 10 strong lensing clusters. We first measured their elongation assuming a given mass–concentration relation. Then, for each cluster, we found the intrinsic shape and orientation which are compatible with the inferred elongation and the measured projected ellipticity. We distinguished two groups. The first one (nearly one-half) seems to be composed of outliers of the mass–concentration relation, which they would fit only if they were characterized by a filamentary structure extremely elongated along the line of sight, that is not plausible considering standard scenarios of structure formations. The second sample supports expectations of *N*-body simulations which prefer mildly triaxial lensing clusters with a strong orientation bias.

Key words: gravitational lensing – methods: statistical – galaxies: clusters: general – cosmology: observations.

1 INTRODUCTION

Clusters of galaxies, the most recent bound structures to form in a hierarchical cold dark matter (CDM) model with a cosmological constant (ΛCDM), offer important clues to the assembly process of structure in the universe. *N*-body simulations are successful in fitting large-scale structure measurements and are able to make detailed theoretical predictions on dark matter halo properties (Navarro, Frenk & White 1997; Bullock et al. 2001; Diemand, Moore & Stadel 2004; Duffy et al. 2008), but some disagreement with observations still persists. One possible conflict between ΛCDM and measurements is the detection of extremely large Einstein radii in massive lensing cluster (Broadhurst & Barkana 2008; Sadeh & Rephaeli 2008; Oguri & Blandford 2009; Zitrin, Broadhurst, Rephaeli & Sadeh 2009). The Einstein radius mirrors the mass contained in the inner regions, and its measurement is quite model-independent. Even if a universal Navarro–Freank–White (NFW) density profile (Navarro, Frenk & White 1996; Navarro et al. 1997) reproduces many characteristics of massive lenses, such haloes should be overconcentrated to fit the data.

The concentration parameter measures the halo central density, which depends on the assembly history and thereby on the time of formation. The halo concentration is then expected to be related to its virial mass, with the concentration decreasing gradually with mass (Bullock et al. 2001). Concentrations of massive galaxy clusters are then a crucial probe of the mean density of the universe at relatively late epochs. State-of-the-art models of cosmic structure formation suggest that galaxy cluster concentrations decrease gradually with virial mass. However, cluster observations have yet to firmly confirm this correlation.

On the observational side, the situation at present is still unclear due to the plurality of methods employed (Comerford & Natarajan 2007). The observed concentration–mass relation for galaxy clusters has a slope consistent with theoretical prediction from simulations, though the normalization factor seems to be higher (Comerford & Natarajan 2007). A critical point is that concentrations measured in massive lensing clusters appear to be systematically larger than X-ray concentrations (Comerford & Natarajan 2007). A similar, though less pronounced, effect is also found in simulations (Hennawi et al. 2007), which show that massive lensing clusters are usually elongated along the line of sight. Oguri & Blandford (2009) showed that the larger the Einstein radius, the larger the overconcentration problem, with clusters looking more massive and concentrated due to the orientation bias.

The overconcentration bias seems to be much larger in observations than in simulations. Broadhurst et al. (2008) inferred significantly high concentrations for four nearly relaxed high-mass

★E-mail: mauro.sereno@polito.it (MS)

clusters. Such a trend has been recently exacerbated with the analysis of the largest known Einstein radius in MACS J0717.5+3745 (Zitrin et al. 2009). Oguri et al. (2009) found that the data from a sample of 10 clusters with strong and weak lensing features were highly inconsistent with the predicted concentration parameters, even including a 50 per cent enhancement to account for the lensing bias (Oguri & Blandford 2009). On the other hand, Okabe et al. (2009) found that the correlation in the c–M relation, as measured in a sample of 19 clusters with significant weak lensing signal that were well fitted by an NFW profile, was marginally compatible with predictions for both slope and normalization.

Different definitions of parameters for spherically averaged profiles can play a role when comparing observations to predictions (Broadhurst & Barkana 2008). Triaxiality issues were addressed by Corless, King & Clowe (2009), who derived weak lensing constraints on three strong lensing clusters without assuming a spherical halo model. The large errors that accompany triaxial parameter estimates can make observations compatible, even if marginally, with theoretical predictions. Investigations in the weak lensing regime demonstrated that neglecting halo triaxiality can lead to over and underestimates of up to 50 per cent and a factor of 2 in halo mass and concentration, respectively (Corless & King 2007). An analysis of AC 114 using only strong lensing data and accounting for triaxiality also supported that projection effects play a major role in the estimate of the concentration (Sereno, Lubini & Jetzer 2009). Finally, analyses of stacked weak lensing clusters of lesser mass do not exhibit the high-concentration problem (Johnston et al. 2007; Mandelbaum, Seljak & Hirata 2008), in agreement with theoretical findings (Oguri & Blandford 2009).

Several effects can play a role: overconcentrated clusters have a larger lensing cross-section (Hennawi et al. 2007); strong lensing clusters preferentially sample the high-mass end of the cluster mass function (Comerford & Natarajan 2007); while extreme cases of triaxiality are rare, such haloes can be much more efficient lenses than their more spherical counterparts (Oguri & Blandford 2009); the strongest lenses in the universe are expected to be a highly biased population preferentially orientated along the line of sight (Hennawi et al. 2007; Oguri & Blandford 2009); estimates of lensing concentrations can be also inflated due to substructures close to the line of sight (Puchwein & Hilbert 2009). On the other hand, contamination of weak lensing catalogues can lead to underestimate the concentration (Limousin et al. 2007).

In order to check the ΛCDM paradigm is then crucial to account for all possible biases when comparing theoretical relations with lensing observations. Such approach was taken in Broadhurst & Barkana (2008), who derived the probability distribution of Einstein radii from concentration distributions found in N-body simulations. Also after considering that lensing clusters are intrinsically overconcentrated and that the inherent triaxiality of CDM haloes along with the presence of substructure enhances the projected mass in some orientations, they found that theoretical predictions are excluded at a 4σ significance. Sadeh & Rephaeli (2008) reached a similar conclusion. They implied the Einstein radius distribution from the probability distribution of cluster formation times and from a formation redshift–concentration scaling derived from N-body simulations. However due to various inherent uncertainties, the statistical range of the predicted distribution may be significantly wider than commonly acknowledged.

Here, we compare measurements with theoretical predictions from semi-analytical investigations and N-body simulations avoiding some possible biases connected to spherical averaging. The paper is as follows. In Section 2, we review the predictions from either N-body simulations or semi-analytical investigations. Section 3 discusses how projected quantities are related to intrinsic parameters for an ellipsoidal cluster. In Section 4, we develop our inversion method which under some given a priori hypotheses allows to infer intrinsic mass, concentration and elongation of a lensing cluster; the method is then applied to a sample of 10 strong lensing clusters. In Section 5, we compare the observed distributions of elongation along the line of sight and ellipticity in the plane of the sky to different theoretical predictions. Section 6 exploits the previously inferred geometrical parameters to predict the intrinsic axial ratios and the orientation of the clusters in the sample. Finally, Section 7 is devoted to a summary and to some final considerations.

Throughout the paper, we assume a flat ΛCDM cosmology with density parameters $\Omega_{\rm M} = 0.3, \Omega_\Lambda = 0.7$ and a Hubble constant $H_0 = 100\,h\,{\rm km\,s^{-1}\ Mpc^{-1}}, h = 0.7$. We quote uncertainties at the 68.3 per cent confidence level.

2 THEORETICAL PREDICTIONS

High-resolution N-body simulations have shown that the density profiles of dark matter haloes are successfully described as NFW density profiles (Navarro et al. 1996, 1997), whose 3D distribution follows

$$\rho_{\rm NFW} = \frac{\rho_{\rm s}}{(r/r_{\rm s})(1+r/r_{\rm s})^2}, \tag{1}$$

where $\rho_{\rm s}$ is the characteristic density and $r_{\rm s}$ is the characteristic length-scale. N-body simulations showed as well that haloes are aspherical and that such profiles can be accurately described by concentric triaxial ellipsoids with aligned axes (Jing & Suto 2002). An NFW equivalent profile whose density is constant on a family of similar, concentric, coaxial ellipsoids is obtained by replacing the spherical radius r with an ellipsoidal radial variable ζ in the intrinsic orthogonal framework centred on the cluster barycentre, and whose coordinates, $x_{i,{\rm int}}$, are aligned with its principal axes,

$$\zeta^2 \equiv \sum_{i=1}^{3} e_{\rm i}^2 x_{i,{\rm int}}^2, \tag{2}$$

where $e_{\rm i}$ are the intrinsic axial ratios. Without loss of generality, we can fix $e_1 \geq e_2 \geq e_3 = 1$. In the following, we will also use the inverse ratios, $0 < q_{\rm i} = 1/e_{\rm i} \leq 1$.

According to recent N-body simulations (Neto et al. 2007; Duffy et al. 2008; Gao et al. 2008; Macciò, Dutton & van den Bosch 2008), the dependence of dark matter halo concentration c on halo mass M and redshift z can be adequately described by a power law

$$c = A(M/M_{\rm pivot})^B(1+z)^C. \tag{3}$$

Since several assumptions were used by competing groups, results can be somewhat different, in particular as far as the overall normalization is concerned. Several values for the linear amplitude of mass fluctuations σ_8 were considered. The higher σ_8, the earlier the formation epoch for haloes of a given mass. Here, we follow Duffy et al. (2008), who used the cosmological parameters from *Wilkinson Microwave Anisotropy Probe* 5 ($\sigma_8 = 0.796$) and found $\{A, B, C\} = \{5.71 \pm 0.12, -0.084 \pm 0.006, -0.47 \pm 0.04\}$ for a pivotal mass $M_{\rm pivot} = 2 \times 10^{12}\,{\rm M}_\odot\,h^{-1}$ in the redshift range 0–2 for their full sample of clusters.

By separately studying the distribution of NFW profile parameters both for the general halo population and for the lensing population (i.e. haloes weighted by their strong lensing cross-section), Hennawi et al. (2007) showed that the distribution of 3D concentrations of the lens population is the same as that of the general halo

population except for a shift upwards by a factor of ∼17 per cent. In the following, we will then also consider an enhanced c–M relation for lensing clusters, with $A \sim 6.68$. Note that such increased value of A could be also seen as due to a larger value of σ_8.

N-body simulations prefer mildly triaxial haloes. Jing & Suto (2002) investigated the probability distribution of intrinsic axial ratios and proposed a universal approximating formula for the distribution of minor to major axis ratios,

$$P(q_1) \propto \exp\left[-\frac{(q_1 - q_\mu/r_{q_1})^2}{2\sigma_s^2}\right], \tag{4}$$

where $q_\mu = 0.54, \sigma_s = 0.113$ and

$$r_{q_1} = (M_{\rm vir}/M_*)^{0.07\Omega_{\rm M}(z)^{0.7}}, \tag{5}$$

with M_* the characteristic non-linear mass at redshift z. The conditional probability for q_2, the ratio of the intermediate to the major axis length, goes as

$$P(q_1/q_2|q_1) = \frac{3}{2(1-r_{\rm min})}\left[1 - \frac{2q_1/q_2 - 1 - r_{\rm min}}{1 - r_{\rm min}}\right] \tag{6}$$

for $q_1/q_2 \geq r_{\rm min} \equiv \max[q_1, 0.5]$, whereas is null otherwise. The lensing population has nearly the same triaxiality distribution as the total cluster population (Hennawi et al. 2007). This could be explained as the result of two counterbalancing effects. Whereas both triaxiality and concentration increase the lensing cross-section, the shape of a dark halo is correlated with its concentration, with more concentrated clusters being more spherical.

For comparison, we will also consider a flat distribution for the axial ratios, such that

$$P(q_1) = 1 \tag{7}$$

for the full range $0 < q_1 \leq 1$ and

$$P(q_2|q_1) = (1 - q_1)^{-1} \tag{8}$$

for $q_2 \geq q_1$ and zero otherwise. The resulting probability for q_2 is then $P(q_2) = \ln(1 - q_2)^{-1}$. Such a flat distribution allows also for very triaxial clusters ($q_1 \lesssim q_2 \ll 1$), which are preferentially excluded by N-body simulations.

Finally, semi-analytical (Oguri & Blandford 2009) and numerical (Hennawi et al. 2007) investigations showed a large tendency for lensing clusters to be aligned with the line of sight. Denoting the angle between the major axis and the line of sight as θ, such condition can be expressed as (Corless et al. 2009)

$$P(\cos\theta) \propto \exp\left[-\frac{(\cos\theta - 1)^2}{2\sigma_\theta^2}\right], \tag{9}$$

with $\sigma_\theta = 0.115$. For comparison, we will also consider a population of clusters randomly oriented, i.e.

$$P(\cos\theta) = 1 \tag{10}$$

for $0 \leq \cos\theta \leq 1$.

3 PROJECTION OF TRIAXIAL HALOES

Dealing with ellipsoidal haloes, we need generalized definitions for the intrinsic NFW parameters. We follow Corless & King (2007), who defined a triaxial virial radius r_{200} such that the mean density contained within an ellipsoid of semimajor axis r_{200} is $\Delta = 200$ times the critical density at the halo redshift; the corresponding concentration is $c_{200} \equiv r_{200}/r_s$. Then, the characteristic overdensity is expressed in terms of c_{200} as for a spherical profile,

$$\delta_c = \frac{200}{3}\frac{c_{200}}{\ln(1 + c_{200}) - c_{200}/(1 + c_{200})}. \tag{11}$$

The virial mass, M_{200}, is the mass within the ellipsoid of semimajor axis r_{200}, $M_{200} = (800\pi/3)q_1 q_2 r_{200}^3 \rho_{\rm cr}$. Such defined c_{200} and M_{200} have small deviations with respect to the parameters computed fitting spherically averaged density profiles, as done in N-body simulations. The only caveat is that the spherical mass obtained in simulations is significantly less than the ellipsoidal M_{200} for extreme axial ratios (Corless & King 2007). However, since the dependence of the concentration on the mass is quite weak, see equation (3), this will have negligible effects on our analysis.

Three rotation angles relate the intrinsic to the observer's coordinate system, i.e. the three Euler's angles, θ, φ and ψ. After alignment of the observer's coordinate system with the direction connecting the observer to the cluster centre, the line of sight has polar angles $\{\theta, \varphi - \pi/2\}$ in the intrinsic system. With a third rotation, ψ, we can properly align the coordinate axes in the plane of the sky. If not stated otherwise, we will line up such axes with the axes of the projected ellipses.

When viewed from an arbitrary direction, quantities constant on similar ellipsoids project themselves on similar ellipses (Stark 1977). In general, the projected map $F_{\rm 2D}$ on the plane of the sky and the intrinsic spheroidal volume density $F_{\rm 3D}$ are related by (Stark 1977; Sereno 2007)

$$F_{\rm 2D}(\xi; l_{\rm P}, p_{\rm i}) = \frac{2}{\sqrt{f}}\int_\xi^\infty F_{\rm 3D}(\zeta; l_{\rm s}, p_{\rm i})\frac{\zeta}{\sqrt{\zeta^2 - \xi^2}}{\rm d}\zeta, \tag{12}$$

where ξ is the elliptical radius in the plane of the sky, $l_{\rm s}$ is the typical length-scale of the 3D density, $l_{\rm P}$ is its projection on the plane of the sky, $p_{\rm i}$ are the other parameters describing the intrinsic density profile (slope, etc.) and f is a function of the cluster shape and orientation,

$$f = e_1^2 \sin^2\theta \sin^2\varphi + e_2^2 \sin^2\theta \cos^2\varphi + \cos^2\theta; \tag{13}$$

the subscript P denotes measurable projected quantities.

Let us see in some details how the parameters describing the projected map depend on the intrinsic shape and orientation of the 3D distribution. The axial ratio of the major to the minor axis of the observed projected isophotes, $e_{\rm P}(\geq 1)$, can be written as (Binggeli 1980),

$$e_{\rm P} = \sqrt{\frac{j + l + \sqrt{(j-l)^2 + 4k^2}}{j + l - \sqrt{(j-l)^2 + 4k^2}}}, \tag{14}$$

where j, k and l are defined as

$$j = e_1^2 e_2^2 \sin^2\theta + e_1^2 \cos^2\theta \cos^2\varphi + e_2^2 \cos^2\theta \sin^2\varphi, \tag{15}$$

$$k = \left(e_1^2 - e_2^2\right)\sin\varphi\cos\varphi\cos\theta, \tag{16}$$

$$l = e_1^2 \sin^2\varphi + e_2^2 \cos^2\varphi. \tag{17}$$

In the following, we will also use the ellipticity $\epsilon = 1 - 1/e_{\rm P}$.

The observed scalelength $l_{\rm P}$ is the projection on the plane of the sky of the cluster intrinsic length (Stark 1977),

$$l_{\rm p} \equiv l_{\rm s}\left(\frac{e_{\rm P}}{e_1 e_2}\right)^{1/2} f^{1/4}. \tag{18}$$

Equation (18) can be rewritten as

$$\frac{l_{\rm s}}{\sqrt{f}} \equiv \frac{l_{\rm P}}{e_\Delta}, \tag{19}$$

where the parameter e_Δ quantifies the elongation of the triaxial ellipsoid along the line of sight (Sereno 2007),

$$e_\Delta = \left(\frac{e_{\rm P}}{e_1 e_2}\right)^{1/2} f^{3/4}. \tag{20}$$

The quantity $l_{\rm P}/e_\Delta$ represents the half-size (along the line of sight) of the ellipsoid as seen from above, i.e. perpendicularly to the line of sight. If $e_\Delta < 1$, then the cluster is more elongated along the line of sight than wide in the plane of the sky. The smaller the e_Δ parameter, the larger the elongation. In the following, we will use as an elongation parameter also a geometrical factor

$$f_{\rm geo} \equiv \frac{(e_1 e_2)^{1/2}}{f^{3/4}} = \frac{e_{\rm P}^{1/2}}{e_\Delta}. \tag{21}$$

Summarizing, the surface density can be expressed in terms of projected quantities as

$$F_{\rm 2D} = \frac{l_{\rm P}}{e_\Delta} f_{\rm 2D}(\xi; e_{\rm P}, \psi; l_{\rm P}; p_{\rm i}, \ldots), \tag{22}$$

where $f_{\rm 2D}$ has the same functional form as for a spherically symmetric halo. In order to write equation (22) in its actual form, we exploited that the integral in ζ in equation (12) is proportional to the intrinsic scalelength $l_{\rm s}$. The dependence on the elongation e_Δ is decoupled from the dependence on the apparent ellipticity and inclination. The other parameters characterizing the 3D profile only account for the radial dependence of the projected density. Then, when we deproject a surface density, the normalization of the volume density can be known only apart from a geometrical factor. Note that in our notation, the elliptical radius is written as a function of the coordinates in the plane of the sky as

$$\xi^2 = \left(x_1^2 + e_{\rm P}^2 x_2^2\right) (l_{\rm s}/l_{\rm P})^2, \tag{23}$$

so that in order to obtain the elliptical projection from the corresponding spherical halo we have (i) to multiply the overall profile by $1/\sqrt{f}$ and (ii) to substitute the polar spherical radius with ξ. The intrinsic scalelength has then to be expressed in terms of the projected one (see equation 19).

4 LENSING INVERSION

For gravitational lensing studies, the projected map of interest is the surface mass density. We will describe the projected NFW density in terms of the strength of the lens $\kappa_{\rm s}$, see equation (24), and of the projected length-scale $r_{\rm sP}$, i.e. the two parameters directly inferred by fitting projected lensing maps. The projected surface mass density Σ of these density profiles is expressed in terms of the convergence κ, i.e. in units of the critical surface mass density for lensing, $\Sigma_{\rm cr} = (c^2\, D_{\rm s})/(4\pi G D_{\rm d} D_{\rm ds})$, where $D_{\rm s}$, $D_{\rm d}$ and $D_{\rm ds}$ are the source, the lens and the lens-source angular diameter distances, respectively. According to our notation in Section 3, for an NFW profile, the intrinsic $l_{\rm s}$ and the projected $l_{\rm P}$ lengths have to be read as $r_{\rm s}$ and $r_{\rm sP}$, respectively.

The central convergence of an NFW profile estimated from lensing can be written in terms of c_{200} and the projected length-scale modulus a factor of $f_{\rm geo}$ (Sereno et al. 2009),

$$\Sigma_{\rm cr} \times \kappa_{\rm s} = \frac{f_{\rm geo}}{\sqrt{e_{\rm P}}} \rho_{\rm s} r_{\rm sP}, \tag{24}$$

where as usual $\rho_{\rm s} = \delta_c \rho_{\rm cr}(z)$ with $\rho_{\rm cr}$ being the critical density of the universe at the cluster redshift. The concentration enters equation (24) through δ_c (see equation 11). The estimate of the mass M_{200} depends also on the scalelength $r_{\rm s}$ which is known modulus a factor of $\sqrt{f}/e_\Delta$ (see equation 19). Then

$$M_{200} = \frac{4\pi}{3} \times 200 \rho_{\rm cr} \times (c_{200} r_{\rm sP})^3 \frac{f_{\rm geo}}{e_{\rm P}^{3/2}}. \tag{25}$$

In order to estimate M_{200} and c_{200} from the projected NFW parameters directly inferred from the lensing analysis, we need to know the elongation of the cluster. The problem is intrinsically degenerate and cannot be solved based on lensing information alone, even in the ideal case of observations without noise. If a cluster is elongated along the line of sight, the concentration parameter and the virial mass estimated from lensing are overestimated (Gavazzi 2005; Oguri et al. 2005). On the other hand, there are more inefficient lensing orientations for a triaxial halo than there are efficient ones (Corless et al. 2009).

4.1 Data sample

We compiled a sample of strong lensing clusters drawing from pre-existing lensing analyses. As selection criteria, we retained only clusters that are well defined by a single dark matter halo and whose lensing data were fitted with an elliptical NFW model. Table 1 lists the final cluster sample, together with corresponding NFW parameters and references to where the lensing analyses were performed. For clusters that do not have published arc/multiple images redshift, we assumed a source redshift $z_{\rm s} = 2.5$. Many input data were originally presented with asymmetric uncertainties. To obtain unbiased estimates, we applied correction formulae for the mean and standard deviation as given by equations (15) and (16) in D'Agostini (2004). Note that there are different definitions for the elliptical radius, which affect the numerical value of the projected scalelength. We took care to translate published data to the notation in the present paper. Furthermore, some studies exploited elliptical NFW potential instead of elliptical mass density. When necessary,

Table 1. The strong lensing cluster data sample.

Name	$z_{\rm d}$	$z_{\rm s}$	$\kappa_{\rm s}$	$r_{\rm sP}(\mathrm{kpc}\,h^{-1})$	ϵ	ref[a]
Abell 1703	0.28	0.888	0.19 ± 0.04	540 ± 90	0.37 ± 0.035	1
MS 2137.3−2353	0.313	1.501	0.67 ± 0.07	112 ± 11	0.226 ± 0.015	2
AC 114	0.315	3.347	0.22 ± 0.02	680 ± 70	0.502 ± 0.018	3
ClG 2244−02	0.33	2.237	0.18 ± 0.02	300 ± 30	0.242 ± 0.015	4
SDSS J1531+3414	0.335	1.096	1.2 ± 0.8	210 ± 110	0.47 ± 0.23	1
SDSS J1446+3032	0.464	–	3.2 ± 2.0	110 ± 50	0.62 ± 0.34	1
MS 0451.6−0305	0.55	0.917	0.28 ± 0.03	350 ± 30	0.425 ± 0.015	4
3C 220.1	0.62	1.49	0.18 ± 0.02	320 ± 30	0.497 ± 0.015	4
SDSS J2111−0115	0.637	–	7.1 ± 1.5	57 ± 11	0.46 ± 0.27	1
MS 1137.5+6625	0.783	–	0.26 ± 0.03	330 ± 30	0.300 ± 0.015	4

Note. References: 1 stands for Oguri et al. (2009); 2 for Gavazzi (2005); 3 for Sereno et al. (2009) and 4 for Comerford et al. (2006). For clusters with multiple image systems, we picked out one source redshift (Column 2). The central convergence $\kappa_{\rm s}$ for the NFW model refers to such redshift; $r_{\rm sP}$ is the projected scalelength.

Table 2. Concentration, mass and elongation for each cluster inferred through lensing inversion assuming as a prior either a standard or an enhanced mass–concentration relation.

Name	Standard c_{200}–M_{200}			Enhanced c_{200}–M_{200}		
	c_{200}	$M_{200}(10^{14}\,\mathrm{M}_\odot\,h^{-1})$	e_Δ	c_{200}	$M_{200}(10^{14}\,\mathrm{M}_\odot\,h^{-1})$	e_Δ
A1703	2.98 ± 0.16	12 ± 4	0.66 ± 0.19	3.46 ± 0.18	13 ± 5	0.91 ± 0.26
MS 2137	3.41 ± 0.13	2.0 ± 0.4	0.068 ± 0.011	3.95 ± 0.15	2.3 ± 0.5	0.093 ± 0.014
AC 114	2.94 ± 0.13	12 ± 3	1.06 ± 0.17	3.40 ± 0.16	14 ± 3	1.44 ± 0.024
ClG 2244−02	3.26 ± 0.13	3.3 ± 0.7	0.69 ± 0.11	3.77 ± 0.15	3.7 ± 0.8	0.95 ± 0.15
SDSS 1531	3.1 ± 0.4	7 ± 7	0.04 ± 0.04	3.6 ± 0.4	8 ± 8	0.06 ± 0.05
SDSS 1446	3.2 ± 0.4	3 ± 3	0.015 ± 0.014	3.7 ± 0.5	3 ± 3	0.020 ± 0.019
MS 0451	2.82 ± 0.13	7.6 ± 1.6	0.29 ± 0.05	3.27 ± 0.15	8.6 ± 1.9	0.40 ± 0.06
3C 220.1	3.03 ± 0.13	2.6 ± 0.6	0.79 ± 0.13	3.51 ± 0.15	2.9 ± 0.6	1.09 ± 0.17
SDSS 2111	3.0 ± 0.2	2.6 ± 1.6	0.004 ± 0.002	3.5 ± 0.2	2.8 ± 1.8	0.006 ± 0.003
MS 1137	2.77 ± 0.13	4.3 ± 0.9	0.71 ± 0.12	3.21 ± 0.15	4.9 ± 1.0	0.97 ± 0.16

Note. Masses are in units of $10^{14}\,\mathrm{M}_\odot\,h^{-1}$.

i.e. for the subsample from Comerford et al. (2006), we converted the potential ellipticity to isodensity ellipticity according to the relation in Golse & Kneib (2002). As a final precaution, we forced errors on κ_s and r_{sP} to be at least of 10 per cent and the error on ϵ to be at least 0.015. Such uncertainties mirror discrepancies among different studies of the same data set [see the analyses of A1703 in Richard et al. (2009) and Oguri et al. (2009) or MS2137.3−2353 in Comerford et al. (2006) and Gavazzi (2005)].

Using the full probability distribution instead of the estimate of mean and error for the ellipticity and the central convergence would be an improvement. However, we limited our method to quite regular clusters (unimodal and well fitted by an NFW profile). From the detailed analyses collected in the literature for each cluster, we found no evidence for complex parameter distributions, with probability functions that are single peaked and generally well behaved.

4.2 Inferred parameters

In order to extract the physical information, i.e. to the determine the parameters c_{200}, M_{200} and e_Δ, we have then to use additional constraints. Since we want to test theoretical predictions, we will employ the prior from the c_{200}–M_{200} relation as given in equation (3). Such an additional third constraint, together with equations (24) and (25), allows us to determine the elongation of the cluster and its mass and concentration. The prior is very strong so the estimated c_{200} and M_{200} will fit nicely the theoretical prediction. On the other hand, e_Δ is free to take whatever value allows the cluster to fit the lensing constraints and the c_{200}–M_{200} relation at the same time. Unphysical values for e_Δ (either $\ll 1$ or $\gg 1$), that would describe more filamentary structures than virialized clusters, will point more to outliers with respect to predictions than to extremely elongated structures. The most likely explanation for extreme e_Δ values is then that the corresponding clusters do not follow the relation imposed a priori. This can be viewed as a sort of proof ab absurdo.

Results are listed in Table 2. We considered both the c_{200}–M_{200} as determined in Duffy et al. (2008) and the case of overconcentrated clusters ($A = 6.68$). To account for measurement errors, we draw lensing parameters (κ_s and r_{sP}) from random normal distributions with mean and dispersion given by the reported central location and scale (see Table 1). Similarly, theoretical uncertainties on the mass–concentration relation were accounted for by drawing the parameters A, B and C, which describe equation (3), from Gaussian distributions with mean and dispersion values found in Duffy et al. (2008). Then, for each set of parameters (κ_s, r_{sP}, A, B and C) we solved the system of equations (3), (24) and (25), discarding only solutions with either $c_{200} > 40$ or $M_{200} > 10^{18}\,\mathrm{M}_\odot\,h^{-1}$. The values listed in Table 2 are the biweight estimators for location and scale of the final inferred distributions (Beers, Flynn & Gebhardt 1990).

If we use the enhanced c_{200}–M_{200} relation, the concentration of each cluster increases by ∼16 per cent, the mass by ∼13 per cent and e_Δ by ∼27 per cent, i.e. the elongation shrinks. Even if clusters come out less elongated if we assume that the lensing population is intrinsically overconcentrated, we see that some outliers are still there. Four out of 10 clusters have $e_\Delta < 0.1$, i.e. the size along the line of sight should be larger than 10 times the maximum length in the plane of the sky. Lensing parameters of SDSS 1531, SDSS 1446 and SDSS 2111 had quite large observational uncertainties which propagate in the estimate of the intrinsic cluster parameters. However, the estimated values of e_Δ are so small that the ordinary value of ∼1 can be excluded for such clusters at a high confidence level. Even doubling the normalization factor of the c–M relation (i.e. assuming $A \sim 11.4$), elongation parameters for two clusters (SDSS 2112 and SDSS 1446) would remain smaller than one-tenth ($e_\Delta \sim 0.019$ and 0.070, respectively).

Note that final results on elongation would have been consistent if we had chosen different methods for deriving the strong lensing parameters. The elongation of A1703 calculated using the data reported in Richard et al. (2009) or Limousin et al. (2008), which both fitted the lensing potential, turns out to be 0.35 ± 0.11 or 0.77 ± 0.17, respectively, the value of e_Δ based on Oguri et al. (2009), that directly fitted the convergence, being intermediate between the two (see Table 2). The elongation of MS 2137 using data in Comerford et al. (2006), that fitted the lensing potential, is 0.051 ± 0.008, compatible with the result based on direct convergence fitting in Gavazzi (2005) (see Table 2). Then, independently of the lensing technique used, results are quite consistent within the errors, both for mildly (A1703) or very elongated (MS 2137) clusters.

It is quite reassuring that whenever a cluster has been analysed either fitting the potential or the convergence, the estimated elongation does not change in a significant way. Together with the central convergence, our method needs only an estimate of the projected ellipticity, which is quite well measured with strong lensing analyses. Golse & Kneib (2002) discussed in detail how potential and surface mass ellipticities are related, and their analysis showed how the mass density ellipticity can be estimated using a previous determination of the potential ellipticity. Once the ellipticity of the surface mass density is known, our method relies only on geometrical projections and is not affected anymore by lensing non-linearities. In fact, we always deproject the surface mass density (instead of the potential) to obtain the intrinsic mass distribution.

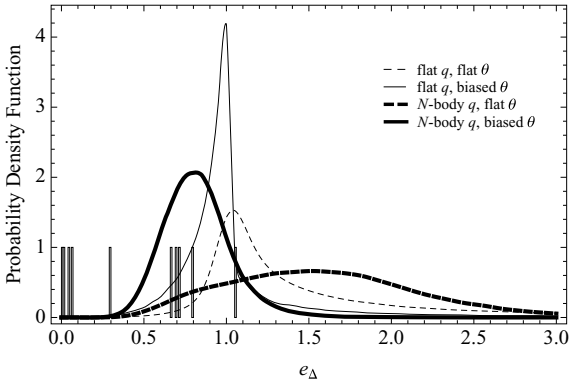

Figure 1. PDFs for the elongations of different cluster populations (see legend). The bars denote the measured values for our full sample assuming a standard c_{200}–M_{200} relation.

5 EXPECTED VERSUS OBSERVED ELONGATION AND ELLIPTICITY

The chance to observe a very elongated cluster can be assessed on a more firm ground. We derived the probability density function (PDF) for a given elongation $P(e_\Delta)$ and a given ellipticity $P(\epsilon)$ under different assumptions. As discussed in Section 3, elongation and ellipticity depend on the intrinsic axial ratios q_1 and q_2 and the orientation angles θ and φ. We considered four scenarios. For the axial ratios, we considered either the N-body predictions in equations (4) and (6) or a flat distribution (see equations 7 and 8). For the alignment, we considered either the biased distribution for $P(\theta)$ in equation (9) or a flat distribution (equation 10). For the azimuth angle φ, we always used a flat distribution, $P(\varphi) =$ constant.

5.1 Elongation

The PDF for the elongation, $P(e_\Delta)$, is plotted in Fig. 1. It is pretty evident that populations of clusters preferentially aligned with the line of sight make a better job to reproduce the observed sample, apart from the group at $e_\Delta < 0.1$. Cumulative distributions are plotted in Fig. 2 and probabilities at very low threshold values are listed in Table 3. Chances for very elongated clusters are very tiny. Even for biased distributions, just one out of few thousands clusters is expected to have $e_\Delta < 0.1$. Even in the most favourable case of a population of clusters biased in θ and flat in axial ratios, the chance to have four out of 10 clusters with $e_\Delta < 0.1$ would be a very tiny 1.7×10^{-16}. So we can conclude that such clusters are very likely outliers of the mass–concentration relations.

Table 3. Probability (in per cent) to have an elongation larger than a given threshold value for different populations of galaxy clusters.

$q_{1,2}$	θ	$P(e_\Delta < 0.1)$ (per cent)	$P(e_\Delta < 0.2)$ (per cent)	$P(e_\Delta < 0.3)$ (per cent)
Flat	Flat	$\lesssim 10^{-3}$	8×10^{-3}	2.7×10^{-3}
Flat	Biased	4.5×10^{-3}	3.5×10^{-2}	1.87×10^{-2}
N-body	Flat	$\lesssim 10^{-3}$	1×10^{-3}	9.5×10^{-3}
N-body	Biased	$\lesssim 10^{-3}$	1.5×10^{-3}	5.7×10^{-2}

Further quantitative comparisons can be performed exploiting the Kolmogorov–Smirnov (KS) test. When we consider the full sample, none of the investigated populations gives a good fit to the data. The better performer, i.e. a population with N-body-like axial ratios and biased alignments, gives a KS significance level of $\lesssim$1 per cent, both for the standard or the enhanced c_{200}–M_{200} relation (see Table 4).

The significance levels improve very significantly when we consider the subsample with $e_\Delta > 0.1$. The prediction from N-body simulations reproduce very well the observed distribution both for the standard (∼31.1 per cent) and the enhanced relation (∼4.7 per cent). For the enhanced relation, also distributions flat in the axial ratios perform well for both populations suffering orientation bias (∼2.1 per cent) or unbiased (∼97.2 per cent).

5.2 Ellipticity

The ellipticity distribution of our sample is not near as informative as the elongation one. PDFs both for unbiased or biased populations have not negligible values in correspondence of the observed ellipticities (see Fig. 3). Populations with flat axial ratios are preferentially rounder ($\epsilon \gtrsim 0$, $e_\Delta \sim 1$) since high values of q_1 are not penalized, but the observed sample does not help to discriminate. The KS test is inconclusive too, see Table 5, even if the biased N-body-like population performs remarkably better considering the $e_\Delta > 0.1$ subsample. However, the ellipticities of such subsample are nothing special. According to a KS test, the ellipticities of the outliers (i.e. clusters with $e_\Delta < 0.1$) might be drawn from the full sample with a significance level ∼98 per cent.

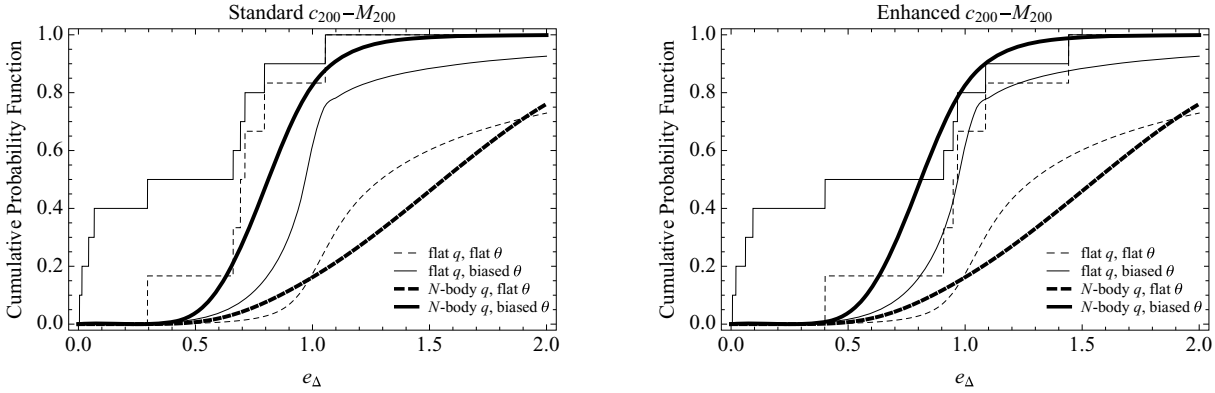

Figure 2. Predicted cumulative distribution functions for elongation versus measurements. The full and dashed step-lines are for the full observed sample and for the clusters with $e_\Delta > 0.1$, respectively; the smooth functions are the predicted distributions under different assumptions (see legends). The left- and right-hand panels show the observed elongations computed assuming either a standard or an enhanced mass–concentration relation, respectively.

Table 4. KS significance level that the elongations of the observed samples of clusters (either all of them or the six with $e_\Delta > 0.1$) are drawn from a given population. We considered e_Δ obtained from either a standard or an enhanced mass–concentration relation.

		Standard c_{200}–M_{200}		Enhanced c_{200}–M_{200}	
$q_{1,2}$	θ	All	$e_\Delta > 0.1$	All	$e_\Delta > 0.1$
Flat	Flat	9×10^{-8}	2.5×10^{-4}	3×10^{-5}	2.1×10^{-1}
Flat	Biased	9×10^{-6}	3.5×10^{-3}	9.3×10^{-3}	9.7×10^{-1}
N-body	Flat	6×10^{-7}	2.5×10^{-4}	5×10^{-5}	9.1×10^{-3}
N-body	Biased	7.8×10^{-3}	3.1×10^{-1}	9.6×10^{-3}	4.7×10^{-2}

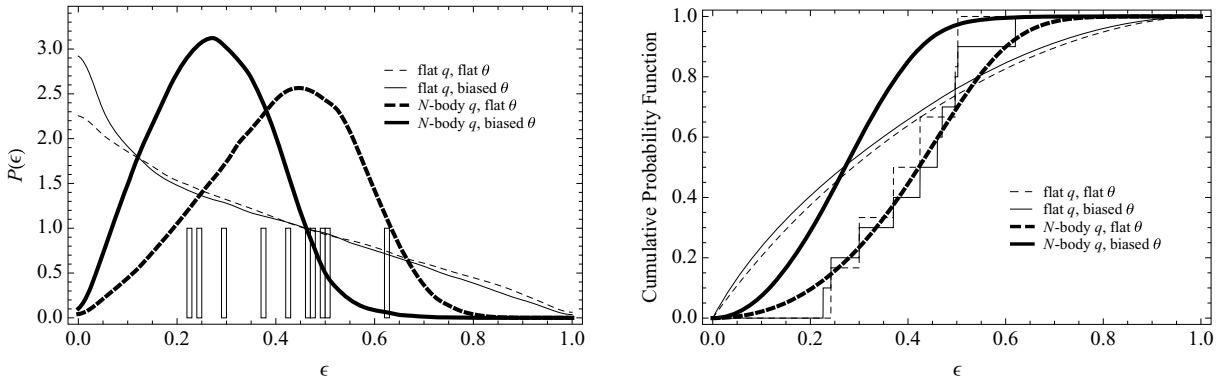

Figure 3. Probability function for the projected ellipticity. Left-hand panel: PDFs for the ellipticity of different cluster populations (see legend). The bars denote the measured values for our full sample. Right-hand panel: predicted cumulative distribution functions for a given elongation versus observations. The full and dashed step-lines are for the full observed sample and for the clusters with $e_\Delta > 0.1$, respectively; the smooth functions are the predicted distributions under different assumptions (see legend).

Table 5. KS significance level that the measured ellipticities of the observed samples of clusters (either all of them or the six with $e_\Delta > 0.1$) are drawn from a given population.

$q_{1,2}$	θ	All	$e_\Delta > 0.1$
Flat	Flat	4.8×10^{-2}	1.5×10^{-2}
Flat	Biased	2.6×10^{-2}	1.0×10^{-2}
N-body	Flat	7.9×10^{-1}	5.9×10^{-1}
N-body	Biased	8.6×10^{-3}	1.2×10^{-1}

Since our sample is neither homogeneous nor statistical, we are cautious in drawing conclusions, but some indications seem to be quite strong. There are a number of clusters whose overconcentration problem cannot be solved just considering some particular geometrical configurations. Even strong biases in intrinsic triaxiality and alignment would not solve the problem. Once such outliers are excluded from the analysis, theoretical predictions are in very good agreement with data. Populations with an alignment bias perform much better than randomly oriented clusters. There is also some evidence for intrinsic axial ratios distributed according to the outputs of *N*-body simulations, even if, under suitable circumstances, flat populations can give good results too.

The assumption that lensing clusters are intrinsically overconcentrated partially reduces the problem, but expected distributions and observations would be compatible with a very low significance level of $\lesssim 1$ per cent, and the problem of having nearly half of the sample with very extreme elongation would be still there. In general, the data analysis performed on our limited sample does not provide evidence for intrinsic overconcentrations, an orientation bias being enough to account for observations of normal clusters ($e_\Delta > 0.1$).

6 INTRINSIC AXIAL RATIOS AND ORIENTATION

Knowledge of the sizes of a cluster in the plane of the sky and along the line of sight allows us to put constraints on its intrinsic geometry (Sereno 2007). However, even exploiting such strong assumptions on the shape, inversion cannot be unique: intrinsically different ellipsoids can cast on the plane of the sky in the same way (Sereno 2007). In order to infer the properties of the cluster and derive its orientation and shape, we have to exploit some external information. We will consider two kinds of prior: first a sharp one which assumes the cluster to be axially symmetric then some less informative priors on the distribution of intrinsic axial ratios for triaxial haloes.

6.1 Axial symmetry

As a working hypothesis, let us first consider if the cluster shape can be approximated as an ellipsoid of revolution. Previous studies have shown that clusters seem to be quite triaxial (De Filippis et al. 2005; Sereno et al. 2006), even if diffuse prolateness cannot be excluded (Plionis, Barrow & Frenk 1991; de Theije, Katgert & van Kampen 1995; Basilakos, Plionis & Maddox 2000; Cooray 2000; Plionis, Basilakos & Tovmassian 2004; Paz et al. 2006). Once the elongation of a cluster is known together with its projected ellipticity, strong constraints can be put on its intrinsic shape (Sereno 2007). Axial symmetry reduces the number of unknown parameters to a couple: a single axial ratio q (≤ 1) and the inclination angle of the symmetry axis i.

A prolate-like solution is admissible when the size along the line of sight is larger than the minimum width in the plane of the sky, that is, when $e_\Delta \leq e_\mathrm{P}$. The intrinsic parameters can be written as $q_1 = q_2 = q$ and $\theta = i$. In terms of the measured quantities

(Sereno 2007),

$$q = \frac{e_\Delta}{e_P^2}, \tag{26}$$

$$\cos i = e_P \sqrt{\frac{e_P^2 - e_\Delta^2}{e_P^4 - e_\Delta^2}}. \tag{27}$$

An oblate-like solution is admissible when the size along the line of sight is smaller than the maximum size in the plane of the sky, that is, when $e_\Delta \geq 1$. According to our notation, for an oblate ellipsoid, $q_1 = q, q_2 = 1$ and $\cos i = \sin\theta \, \sin\varphi$. Inversion gives (Sereno 2007)

$$q = \frac{1}{e_P e_\Delta}, \tag{28}$$

$$\cos i = \sqrt{\frac{e_\Delta^2 - 1}{e_P^2 e_\Delta^2 - 1}}. \tag{29}$$

The prolate and the oblate solutions are admissible at the same time only when the size along the line of sight is intermediate, i.e. $1 \leq e_\Delta \leq e_P$.

Results of the inversion are listed in Table 6. Intrinsic parameters have been obtained by means of equations (26) and (27) for the prolate case and equations (28) and (29) for the oblate case. Input values for elongation and ellipticity were randomly extracted from normal distributions centred in the measured value and with dispersion equal to the observational uncertainty. The values listed in Table 6 are the biweight estimators of the final distributions of the inferred parameters. The significance level for a given shape has been obtained as the fraction of drawn e_P and e_Δ for which a given compatibility condition is fulfilled. We considered only elongation values obtained assuming a standard mass–concentration relation. The prolate hypothesis is compatible with the full sample, but the shapes should be extremely long and narrow ($q \lesssim 0.35$) and nearly perfectly aligned with the line of sight ($\cos i \gtrsim 0.88$). The conclusion that clusters with $e_\Delta < 0.1$ are outliers is further stressed by the very small space volume allowed for the intrinsic parameters (under wrong hypotheses, uncertainties are very likely to be very small).

A population of oblate clusters do not provide a good description of the data. Only a tiny region in the parameter space of elongation and ellipticity allowed by the data is compatible with such a hypothesis. Only AC 114, with $e_\Delta \sim 1$, has a good chance to be described by an oblate shape (∼60 per cent), otherwise significance levels are $\lesssim$5 per cent. For the few clusters for which oblateness is marginally compatible, inclination angles would still be biased, symmetry axis being nearly perpendicular to the line of sight ($\cos i \lesssim 0.26$), whereas intermediate axial ratios would be preferred ($0.43 \lesssim q \lesssim 0.74$).

6.2 Triaxial clusters

In order to exactly determine the intrinsic shape of a triaxial cluster, we should know both ellipticity and elongation together with two additional observational constraints. The problem of inverting a projected map is intrinsically degenerate and even adding X-ray observations or measurements of the Sunyaev–Zeldovich effect would not make the inversion unique (Sereno 2007). An alternative approach is to use priors on the intrinsic parameters (Corless et al. 2009). Here, we try to solve the system of equations:

$$\begin{aligned} e_P &= e_P(q_1, q_2; \theta, \varphi); \\ e_\Delta &= e_\Delta(q_1, q_2; \theta, \varphi) \end{aligned} \tag{30}$$

using a couple of proxies for the axial ratios. In particular, we exploit either a flat distribution or the guess from N-body simulations. Operatively, we randomly extract the axial ratios from the assumed prior distribution and then solve for θ and φ in equations (30). For each iteration, a couple of input values for e_P and e_Δ are also randomly drawn. If there is a solution to the system, we consider the drawn q_1 and q_2 and the corresponding θ and φ to be a sample from the posterior distribution.

Results are listed in Table 7, where as usual we reported biweight estimators. Final estimates are quite insensitive to the priors. This asserts the validity of our inversion approach, since a Bayesian analysis is effective as far as the effect of priors is as not informative as possible. The parameter space for solutions is quite narrow for very elongated clusters ($e_\Delta < 0.3$), and we actually were able to find very few of them, less than one out of 10 000 drawings. Assuming the sharp prolate prior on the shape, we could find some extremely elongated configurations, but such intrinsic shapes are pretty much excluded by assuming more realistic priors on the axial distributions as the ones expected for general triaxial configurations. This further suggests that our sample contains several outliers of the mass–concentration relation.

Posterior probabilities for A1703, AC 114, ClG 2244, 3C 220 and MS 1137 are plotted in Figs 4–8, respectively. The final distributions have been smoothed using a Gaussian kernel estimator with reflective boundary conditions (Vio et al. 1994; Ryden 1996). For each cluster, whatever the prior on the axial ratios, the posterior

Table 6. Intrinsic parameters (axial ratio q and inclination angle i) assuming either prolateness or oblateness.

	Prolate			Oblate		
Name	Comp.	q	$\cos i$	Comp.	q	$\cos i$
A1703	∼1	0.26 ± 0.08	0.94 ± 0.04	0.0342	0.59 ± 0.05	0.25 ± 0.11
MS 2137	∼1	0.040 ± 0.007	0.9994 ± 0.0002	$\lesssim 10^{-5}$	NA	NA
AC 114	∼1	0.26 ± 0.05	0.88 ± 0.05	0.622	0.43 ± 0.04	0.26 ± 0.09
ClG 2244−02	∼1	0.40 ± 0.07	0.93 ± 0.03	2.31×10^{-3}	0.74 ± 0.03	0.24 ± 0.12
SDSS 1531	∼1	0.012 ± 0.011	0.999795 ± 0.0002	$\lesssim 10^{-5}$	NA	NA
SDSS 1446	∼1	0.0014 ± 0.0014	0.999989 ± 0.000015	$\lesssim 10^{-5}$	NA	NA
MS 0451	∼1	0.098 ± 0.017	0.9902 ± 0.003	$\lesssim 10^{-5}$	NA	NA
3C−220.1	∼1	0.20 ± 0.03	0.94 ± 0.02	0.0542	0.48 ± 0.02	0.16 ± 0.07
SDSS 2111	∼1	0.0010 ± 0.0009	0.999998 ± 10^{-6}	$\lesssim 10^{-5}$	NA	NA
MS 1137	∼1	0.35 ± 0.06	0.93 ± 0.03	6.45×10^{-3}	0.68 ± 0.03	0.23 ± 0.11

Note. The column 'Comp.' gives the significance level for a cluster shape to be compatible with a given set of data. For a very low compatibility with a given shape hypothesis, parameter values are not available (NA).

Table 7. Intrinsic parameters for a triaxial shape (axial ratios, q_1 and q_2, and orientation angles θ and φ) inferred using different priors for the intrinsic axial ratio distributions.

		N-body q					Flat q			
Name	Comp.	q_1	q_2	$\cos\theta$	$\cos\varphi$	Comp.	q_1	q_2	$\cos\theta$	$\cos\varphi$
A1703	0.094	0.39 ± 0.07	0.55 ± 0.11	0.87 ± 0.10	0.81 ± 0.16	0.025	0.37 ± 0.10	0.61 ± 0.15	0.90 ± 0.09	0.76 ± 0.17
MS 2137.3	$\lesssim 10^{-4}$			NA		$\lesssim 10^{-4}$			NA	
AC 114	0.104	0.36 ± 0.06	0.52 ± 0.13	0.77 ± 0.11	0.93 ± 0.07	0.054	0.31 ± 0.09	0.61 ± 0.18	0.84 ± 0.12	0.85 ± 0.13
ClG 2244	0.149	0.43 ± 0.06	0.57 ± 0.08	0.93 ± 0.04	0.67 ± 0.20	0.026	0.45 ± 0.10	0.60 ± 0.12	0.92 ± 0.05	0.67 ± 0.22
SDSS 1531	1.2×10^{-3}	0.44 ± 0.06	0.60 ± 0.10	0.82 ± 0.25	0.70 ± 0.17	4.3×10^{-4}	~ 0.26	~ 0.49	~ 0.83	~ 0.60
SDSS 1446	1.7×10^{-4}	~ 0.45	~ 0.70	~ 0.65	~ 0.39	1.7×10^{-4}	~ 0.16	~ 0.76	~ 0.75	~ 0.63
MS 0451.6	$\lesssim 10^{-4}$			NA		3×10^{-4}	~ 0.14	~ 0.27	~ 0.99	~ 0.64
3C 220.1	0.037	0.33 ± 0.06	0.50 ± 0.12	0.85 ± 0.07	0.95 ± 0.05	0.025	0.29 ± 0.09	0.56 ± 0.15	0.92 ± 0.06	0.86 ± 0.13
SDSS 2111	$\lesssim 10^{-4}$			NA		$\lesssim 10^{-4}$			NA	
MS 1137.5	0.174	0.38 ± 0.05	0.52 ± 0.08	0.92 ± 0.04	0.74 ± 0.16	0.028	0.41 ± 0.09	0.59 ± 0.12	0.92 ± 0.06	0.73 ± 0.19

Note. The column 'Comp.' gives the significance level for a cluster shape to be compatible with a given set of data.

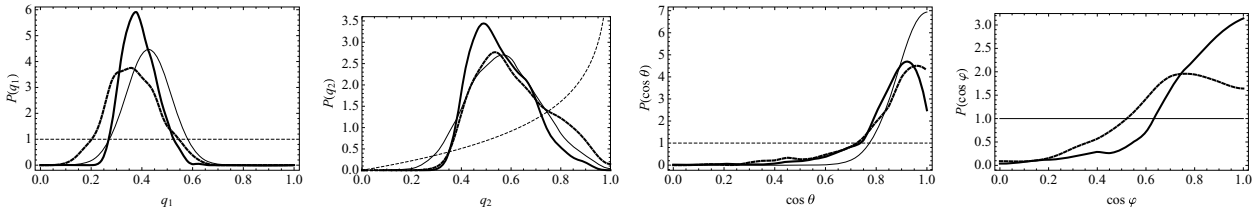

Figure 4. Posterior PDFs for the intrinsic parameters of A1703. Panels from the left to the right are for the PDF of $q_1, q_2, \cos\theta$ and $\cos\varphi$, respectively. Full and dashed thick lines have been obtained assuming an N-body-like and a flat prior on the axis ratios, respectively. The full and dashed thin lines in the left-hand panel represent the N-body and the flat prior for $P(q_1)$, respectively; the full and dashed thin lines in the q_2 panel represent the prior distributions according to either an N-body or a flat prior, respectively; the thin and dashed full line in the $\cos\theta$ panel represent the biased and the flat distributions on the orientation angle. Such priors on $\cos\theta$ were not used to derive the PDFs. Finally the flat line in the $\cos\varphi$ panel represents a uniform distribution.

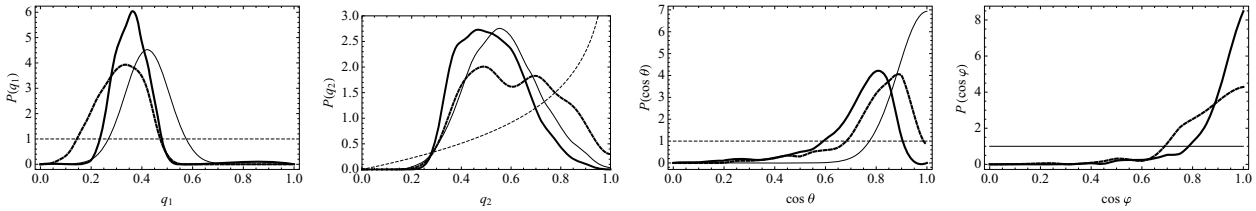

Figure 5. The same as Fig. 4 for the cluster AC 114.

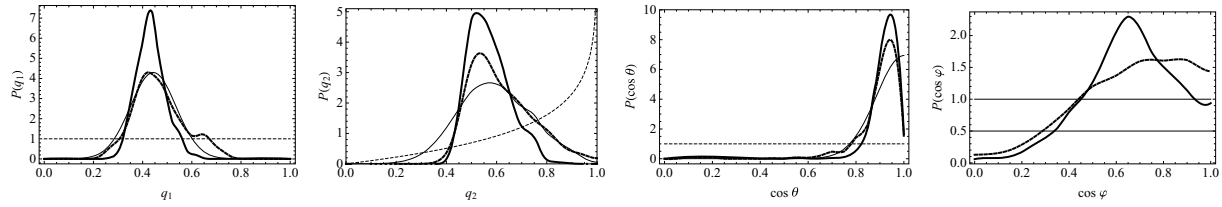

Figure 6. The same as Fig. 4 for the cluster ClG 2244.

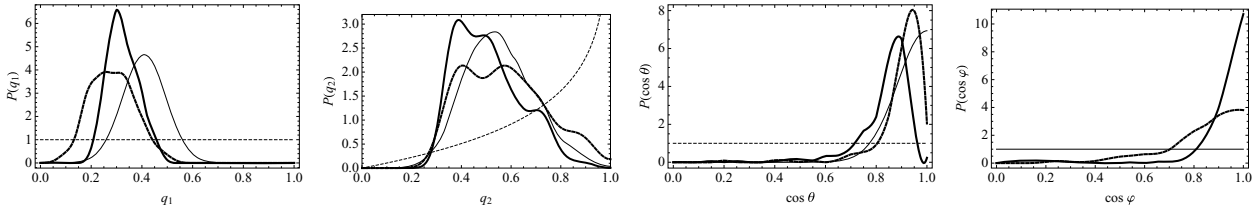

Figure 7. The same as Fig. 4 for the cluster 3C 220.

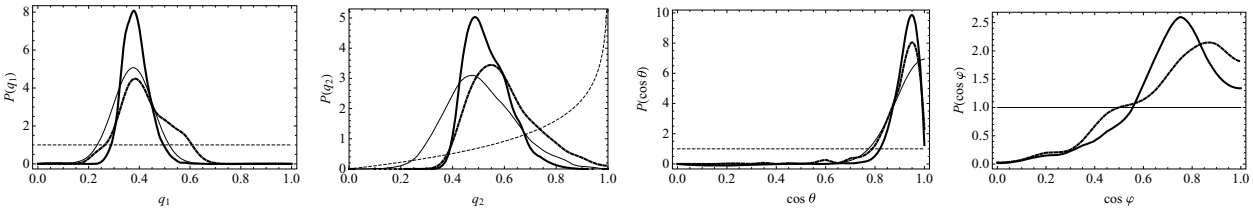

Figure 8. The same as Fig. 4 for the cluster MS 1137.

probabilities are quite similar. Even if we assume a flat distribution for the axial ratios, the posterior probability is quite similar to the prediction from *N*-body simulations. Note that the alignment bias is confirmed by the above analysis without any prior assumption on the orientation.

7 DISCUSSION

Recent observational analyses have been finding many lensing clusters with Einstein radii much larger than expected in a standard ΛCDM model (Broadhurst et al. 2008; Oguri et al. 2009). We performed a statistical analysis on a sample of 10 clusters that were well fitted by a single NFW model. Our method was as follows. We supposed theoretical expectations from *N*-body simulations to be true and modelled clusters as NFW haloes fitting standard mass–concentration relations. Then, we found the elongation along the line of sight of the clusters required to satisfy at the same time both lensing data and theoretical predictions. Finally, we studied for each cluster which intrinsic shape and orientation were compatible with the inferred elongation and the measured projected ellipticity. At each step, we checked the exploited hypothesis ab absurdo by finding any inconsistency between theoretical predictions and actual conditions under which expectations can be in agreement with data.

We first considered the inferred distribution of elongations, comparing that with the probability to really see them observing a given population. We found two groups in our sample. The first group is in very good agreement with what expected from a population of clusters fitting the mass–concentration relation and preferentially oriented along the line of sight, as suggested by theoretical analyses of lensing clusters (Hennawi et al. 2007; Oguri & Blandford 2009). Observed ellipticities and inferred elongations are also in agreement with intrinsic axial ratios following distributions derived in *N*-body simulations. There is no evidence for such lensing clusters to be intrinsically overconcentrated even if data cannot exclude that.

The second subsample in our analysis is made of clusters very likely to be outliers of the mass–concentration relation. To fulfil the expected relation, they should develop along the line of sight as a filamentary structure with extreme elongation, a clearly poor description for massive haloes. Even allowing for more concentrated haloes for a given mass by enhancing the *c*–*M* relation, elongations would still be extreme.

Even if our sample was not statistical, we took care of selecting quite regular clusters. However, bimodal structures nearly aligned with the line of sight would seemingly have a regular morphology in the plane of the sky. Such configurations would boost the apparent concentration, but they are very rare and it is problematic to consider all of our outliers within this scenario. Furthermore, we used a mass–concentration relation derived for the full sample of clusters, not just the virialized and regular ones.

The second step in our analysis further strengthens such view. Using a series of statistical priors, we found for each one of the mildly elongated clusters an intrinsic structure and orientation compatible with the inferred elongation. Prolate shapes make a better work in explaining data than oblate clusters, but in general data are fully compatible with triaxial structures. Whatever the hypothesis exploited as prior on the intrinsic axial ratios, inferred intrinsic parameters suggest mildly triaxial clusters with an alignment bias in very good agreement with expectations from *N*-body simulations.

An alternative approach would have been to apply the fitting procedure to inclined triaxial haloes in the first place. As far as the estimates of the projected ellipticity and of the central convergence are not biased, our method should be able to fully explore the space of the triaxial parameters (shape and orientation). In fact, given a projected map, we consider all the intrinsic configurations compatible with data. This is done through equations (14) and (24). Such set of equations allows us to study the full intrinsic parameter space, even in case of disjoint regions compatible with data.

Either projecting intrinsic parameters and fitting to the lensing data or fitting projected maps and then deprojecting (as done in this paper) should give the same final result. In fact, in a pure lensing analysis the triaxial structure of a cluster is constrained only by its projected map, so that both procedures should pick out the same sets of intrinsic parameters that can fit the measured quantities, i.e. ellipticity, orientation and central surface density.

ACKNOWLEDGMENTS

For the first stages of this work, MS was supported by the Swiss National Science Foundation and the Tomalla Foundation.

REFERENCES

Basilakos S., Plionis M., Maddox S. J., 2000, MNRAS, 316, 779
Beers T. C., Flynn K., Gebhardt K., 1990, AJ, 100, 32
Binggeli B., 1980, A&A, 82, 289
Broadhurst T. J., Barkana R., 2008, MNRAS, 390, 1647
Broadhurst T., Umetsu K., Medezinski E., Oguri M., Rephaeli Y., 2008, ApJ, 685, L9
Bullock J. S., Kolatt T. S., Sigad Y., Somerville R. S., Kravtsov A. V., Klypin A. A., Primack J. R., Dekel A., 2001, MNRAS, 321, 559
Comerford J. M., Natarajan P., 2007, MNRAS, 379, 190
Comerford J. M., Meneghetti M., Bartelmann M., Schirmer M., 2006, ApJ, 642, 39
Cooray A. R., 2000, MNRAS, 313, 783
Corless V. L., King L. J., 2007, MNRAS, 380, 149
Corless V. L., King L. J., Clowe D., 2009, MNRAS, 393, 1235
D'Agostini G., 2004, preprint (astro-ph/0403086)
De Filippis E., Sereno M., Bautz M. W., Longo G., 2005, ApJ, 625, 108
de Theije P. A. M., Katgert P., van Kampen E., 1995, MNRAS, 273, 30
Diemand J., Moore B., Stadel J., 2004, MNRAS, 353, 624
Duffy A. R., Schaye J., Kay S. T., Dalla Vecchia C., 2008, MNRAS, 390, L64
Gao L., Navarro J. F., Cole S., Frenk C. S., White S. D. M., Springel V., Jenkins A., Neto A. F., 2008, MNRAS, 387, 536
Gavazzi R., 2005, A&A, 443, 793
Golse G., Kneib J.-P., 2002, A&A, 390, 821

Hennawi J. F., Dalal N., Bode P., Ostriker J. P., 2007, ApJ, 654, 714
Jing Y. P., Suto Y., 2002, ApJ, 574, 538
Johnston D. E. et al., 2007, preprint (arXiv: 0709.1159)
Limousin M. et al., 2007, ApJ, 668, 643
Limousin M. et al., 2008, A&A, 489, 23
Macciò A. V., Dutton A. A., van den Bosch F. C., 2008, MNRAS, 391, 1940
Mandelbaum R., Seljak U., Hirata C. M., 2008, J. Cosmol. Astropart. Phys., 8, 6
Navarro J. F., Frenk C. S., White S. D. M., 1996, ApJ, 462, 563
Navarro J. F., Frenk C. S., White S. D. M., 1997, ApJ, 490, 493
Neto A. F. et al., 2007, MNRAS, 381, 1450
Oguri M., Blandford R. D., 2009, MNRAS, 392, 930
Oguri M., Takada M., Umetsu K., Broadhurst T., 2005, ApJ, 632, 841
Oguri M. et al., 2009, ApJ, 699, 1038
Okabe N., Takada M., Umetsu K., Futamase T., Smith G. P., 2009, preprint (arXiv:0903.1103)
Paz D. J., Lambas D. G., Padilla N., Merchán M., 2006, MNRAS, 366, 1503
Plionis M., Barrow J. D., Frenk C. S., 1991, MNRAS, 249, 662
Plionis M., Basilakos S., Tovmassian H. M., 2004, MNRAS, 352, 1323
Puchwein E., Hilbert S., 2009, MNRAS, 398, 1298
Richard J., Pei L., Limousin M., Jullo E., Kneib J. P., 2009, A&A, 498, 37
Ryden B. S., 1996, ApJ, 461, 146
Sadeh S., Rephaeli Y., 2008, MNRAS, 388, 1759
Sereno M., 2007, MNRAS, 380, 1207
Sereno M., De Filippis E., Longo G., Bautz M. W., 2006, ApJ, 645, 170
Sereno M., Lubini M., Jetzer P., 2009, preprint (arXiv:0904.0018)
Stark A. A., 1977, ApJ, 213, 368
Vio R., Fasano G., Lazzarin M., Lessi O., 1994, A&A, 289, 640
Zitrin A., Broadhurst T., Rephaeli Y., Sadeh S., 2009, ApJL, 707, 102

This paper has been typeset from a TEX/LATEX file prepared by the author.